Discover Oncology

Analysis

Machine learning explores the prognostic and immuno-oncological impact of mitochondrial unfolded protein response in CESC

Keh-Sen Liu[1,2] · Yen-Hsiang Chang[3] · Hsing-Ju Wu[2,4] · Hung-Yu Lin[4,5]

Received: 18 February 2025 / Accepted: 15 May 2025
Published online: 23 May 2025
© The Author(s) 2025 OPEN

Abstract

Background Cervical squamous cell carcinoma and endocervical adenocarcinoma (CESC) pose significant global health challenges. While the mitochondrial unfolded protein response (UPR^{mt}) is known to influence cancer biology, its specific role in CESC remains unclear.

Methods We employed machine learning to analyze UPR^{mt} genes in CESC using TCGA multi-omics data. Our comprehensive analysis included genetic alterations, prognostic significance, tumor-immune interactions, single-cell transcriptomics, pathway enrichment, and drug sensitivity assessments.

Results *ATF5* emerged as the most significant prognostic factor among UPR^{mt} genes, with high expression correlating with better overall survival. High *ATF5* expression was associated with an immunologically active tumor microenvironment, characterized by enhanced immune cell infiltration, increased immune checkpoint expression, and higher tumor mutational burden. Single-cell RNA sequencing revealed *ATF5*'s distinct expression patterns in stromal cells, particularly in endometrial stromal and smooth muscle cells. Gene set enrichment analysis provided mechanistic insight, revealing *ATF5*'s connection to the immune response via the regulation of P-stalk ribosome functions, a finding that underscores a novel aspect of UPR^{mt}'s role in shaping the tumor immune landscape. Drug sensitivity analysis showed that low *ATF5* expression correlated with resistance to conventional chemotherapeutics (cisplatin, paclitaxel, and etoposide) but increased sensitivity to imatinib, potentially through *EP300*-dependent mechanisms.

Conclusions Our findings establish *ATF5* as both a favorable prognostic marker and a key immune response regulator in CESC. Its influence on the tumor microenvironment and treatment response suggests potential therapeutic applications. These insights into UPR^{mt}'s role in CESC provide new directions for developing personalized treatment strategies.

Keywords Activating transcription factor 5 · Cervical cancer · Mitochondrial unfolded protein response · Tumor microenvironment · Machine learning · Drug sensitivity

Keh-Sen Liu and Yen-Hsiang Chang contributed equally to this work.

Supplementary Information The online version contains supplementary material available at https://doi.org/10.1007/s12672-025-02723-9.

✉ Hung-Yu Lin, linhungyu700218@gmail.com | [1]Division of Infectious Diseases, Department of Internal Medicine, Show Chwan Memorial Hospital, Changhua 500, Taiwan. [2]Department of Nursing, Jenteh Junior College of Medicine, Nursing and Management, Miaoli 356, Taiwan. [3]Department of Nuclear Medicine, Kaohsiung Chang Gung Memorial Hospital and Chang Gung University College of Medicine, Kaohsiung 833, Taiwan. [4]Research Assistant Center, Show Chwan Memorial Hospital, Changhua 500, Taiwan. [5]Department of Post-Baccalaureate Medicine, College of Medicine, National Chung Hsing University, Taichung 402, Taiwan.

1 Introduction

Cervical squamous cell carcinoma and endocervical adenocarcinoma (CESC) remain significant global health challenges, particularly in developing countries [1]. Despite advances in prevention and treatment strategies, the molecular mechanisms underlying CESC progression and therapeutic resistance are not fully understood. Recent evidence suggests that mitochondrial dysfunction and subsequent stress responses play crucial roles in cancer development and progression [2].

The mitochondrial unfolded protein response (UPR^{mt}) is a conserved cellular stress response pathway that maintains mitochondrial proteostasis and function [3, 4]. This pathway is activated when misfolded proteins accumulate in the mitochondria, triggering a retrograde signaling cascade that induces the expression of nuclear-encoded mitochondrial chaperones and proteases. Key players in the UPR^{mt} pathway include transcription factors [Activating Transcription Factor 4 (*ATF4*), Activating Transcription Factor 5 (*ATF5*), Nuclear Respiratory Factor 1 (*NRF1*), Nuclear Factor Erythroid 2-Related Factor 2 (*NFE2L2*)], mitochondrial proteases [Caseinolytic Mitochondrial Matrix Peptidase Proteolytic Subunit (*CLPP*), Lon Peptidase 1 (*LONP1*)], chaperones [Heat Shock Protein Family A Member 9 (*HSPA9*), Heat Shock Protein Family D Member 1 (*HSPD1*)], and proteins involved in mitochondrial dynamics [Optic Atrophy 1 (*OPA1*), Mitofusin 1 and 2 (*MFN1*, *MFN2*), Dynamin 1 Like (*DNM1L*)].

The role of UPR^{mt} components, particularly *ATF5*, has shown remarkable complexity across different cancer types. In glioblastoma and breast cancer, *ATF5* has been reported to promote cancer cell survival and proliferation, functioning as an oncogenic factor [5]. Moreover, *ATF5* activates the expression of its pro-invasion downstream targets, including the collagen receptor integrin *α2β1* genes, *ITGα2* and *ITGβ1*, which interact with collagen type I, E-cadherin, and matrix metalloproteinase to drive tumor invasion in various human cancer cell lines, such as lung, breast, cervical, gastric, fibrosarcoma, and pancreatic cancers [5]. Conversely, *ATF5* is markedly downregulated due to promoter methylation, and restoring *ATF5* expression can suppress the growth of hepatocellular carcinoma (HCC) cells [6]. Furthermore, lower *ATF5* levels have been linked to higher tumor malignancy and hold potential as a prognostic marker in HCC [7]. This context-dependent duality of *ATF5* function highlights the need for cancer-specific investigation of UPR^{mt} components. In CESC, despite the established importance of mitochondrial function in cervical cancer progression, the specific role of *ATF5* and other UPR^{mt} components remains largely unexplored, particularly in relation to immune regulation and treatment response.

The emergence of machine learning approaches in oncology has revolutionized our ability to analyze complex molecular datasets and identify clinically relevant patterns. These computational methods enable the systematic evaluation of multiple genes within a pathway to determine their relative importance in disease progression and patient outcomes. In the context of UPR^{mt}, machine learning algorithms can help prioritize key molecular players for detailed investigation, potentially uncovering novel therapeutic targets.

While individual components of the UPR^{mt} pathway have been studied in various cancers, a comprehensive analysis of their collective role in CESC remains unexplored. Moreover, the relationship between UPR^{mt} genes and the tumor immune microenvironment, as well as their impact on treatment response, requires further investigation. Understanding these relationships could provide valuable insights into potential therapeutic strategies for CESC treatment.

In this study, we employed a systematic approach as illustrated in Fig. 1. First, we performed a comprehensive examination of UPR^{mt} genetic alterations and their impact on patient prognosis, along with their ability to discriminate between normal and tumor tissues. Subsequently, we implemented a machine learning approach to systematically evaluate and rank the prognostic significance of UPR^{mt} genes in CESC, which led to the identification of the most critical gene within this pathway. We then conducted an in-depth characterization of this key player through multiple approaches: analysis of its impact on the tumor immune microenvironment, single-cell RNA sequencing to map its cellular distribution and interactions, functional pathway enrichment analysis to understand its biological roles, and pharmacogenetic studies to evaluate its influence on treatment responses. This comprehensive investigation aims to provide novel insights into the role of UPR^{mt} in CESC progression and its potential therapeutic implications.

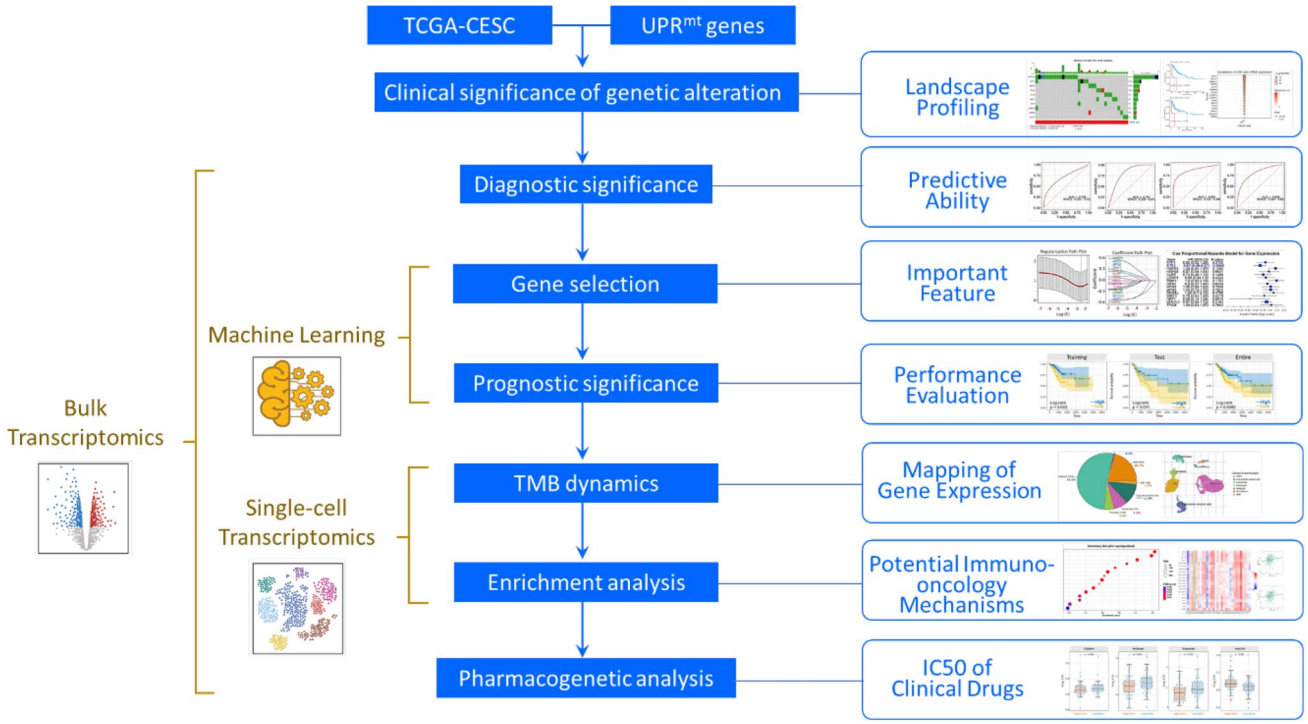

Fig. 1 Schematic workflow of the study design and analytical approaches used to investigate UPR^{mt} genes in CESC

2 Methods

2.1 Data acquisition and preprocessing

Clinical and genetic data for cervical squamous cell carcinoma and endocervical adenocarcinoma (CESC) were obtained from the UCSC Xena platform (https://xena.ucsc.edu/). The dataset included mRNA expression profiles, mutation data, and clinical outcomes for patients diagnosed with CESC. Data preprocessing involved several steps to ensure the quality and reliability of the analyses. First, mRNA expression data were normalized using the transcripts per million (TPM) method to account for differences in sequencing depth and gene length. Samples with incomplete clinical information, such as missing survival data or demographic details, were excluded from the analysis. Copy number variation (CNV) data were also retrieved and processed to evaluate their correlation with mRNA expression levels. CNV data were categorized into amplifications, deletions, and neutral states, and their impact on gene expression was assessed using Spearman's correlation analysis. Immunohistochemistry data were accessed from the Human Protein Atlas (https://www.proteinatlas.org/) [8, 9].

2.2 Genetic alteration and survival analysis

To investigate the genetic alterations of UPR^{mt} genes in CESC, we utilized the Gene Set Cancer Analysis (GSCA) platform (https://guolab.wchscu.cn/GSCA/#/) [10]. This platform enabled the identification of mutation frequencies and CNV patterns for UPR^{mt} genes, including *NFE2L2*, *OPA1*, *MFN2*, *TFAM*, *ATF4*, *NRF1*, *ATF5*, *DNM1L*, *HSPA9*, *MFN1*, *CLPP*, *PRKN*, and *LONP1*. Kaplan–Meier survival analysis was performed to evaluate the association between genetic alterations and patient outcomes, including overall survival (OS) and progression-free survival (PFS). Log-rank tests were used to determine the statistical significance of survival differences between groups with and without specific genetic alterations. Additionally, the relationship between CNV and mRNA expression levels was visualized using scatter plots, and genes with significant correlations were highlighted.

Fig. 2 Genetic profiling and clinical significance of UPR^{mt} genes in CESC patients. **A** Oncoplot exhibiting alteration frequency and types of single nucleotide variant (SNV) in UPR.^{mt} genes and tumor mutation burden (TME). **B**–**C** Kaplan–Meier analysis of the overall survival (OS) probability (**B**) and progression-free survival (PFS) probability (**C**) between patients harboring wild-type (WT) *ATF4* and mutant *ATF4*. **D** Bubble plot depicting Spearman correlation of copy number variation (CNV) with mRNA expression. FDR, false discovery rate. **E**–**T** Scatter plots representing Spearman correlation of CNV with mRNA expression for *ATF4* (**E**), *CLPP* (**F**), *HSPA9* (**G**), *ATF5* (**H**), *DNM1L* (**I**), *HSPD1* (**J**), *LONP1* (**K**), *MFN1* (**L**), *MFN2* (**M**), *NFE2L2* (**N**), *NRF1* (**O**), *OPA1* (**P**), *PINK1* (**Q**), *SIRT3* (**R**), *TFAM* (**S**), and *PRKN* (**T**). 'Cor' denoting Spearman rank correlation coefficient. FDR, false discovery rate. **U**–**X** Kaplan–Meier analysis of the OS probability (**U**, **W**) and PFS probability (**V**, **X**) stratified by amplification (Amp), deletion (Dele) and wild-type (WT) of *CLPP* or *LONP1*

2.3 Machine learning for prognostic gene selection

To identify genes with the most significant prognostic value, we employed the least absolute shrinkage and selection operator (LASSO) regression algorithm. This analysis was conducted using the "glmnet" package in R. The LASSO algorithm was applied to the training dataset to select genes that were most predictive of survival outcomes while minimizing overfitting. The optimal regularization parameter (λ) was determined using tenfold cross-validation. Genes with non-zero coefficients at the optimal lambda value were considered significant and were further analyzed using Cox proportional hazards regression to evaluate their independent prognostic value. Receiver operating characteristic (ROC) curves were generated for each gene to assess their ability to distinguish tumor tissues from normal tissues. The area under the curve (AUC) was calculated to quantify the discriminatory performance of each gene. For the LASSO regression analysis, we employed a 7:3 ratio for training and test set splitting, where 70% of the samples were used for model training and 30% for model validation. The training set was used to build the LASSO model and identify key features, while the test set was used to validate the model's performance. We performed tenfold cross-validation within the training set to optimize the lambda parameter and prevent overfitting. The final model was selected based on the lambda value that minimized the mean cross-validated error.

2.4 Tumor-immune microenvironment analysis

The tumor-immune microenvironment was characterized using a combination of TCGAplot (https://bmcbioinformatics.biomedcentral.com/articles/https://doi.org/10.1186/s12859-023-05615-3) [11] and CAMOIP (https://academic.oup.com/bib/article/23/3/bbac129/6565619) [12]. Stromal, immune, and ESTIMATE scores were calculated for each sample to evaluate tumor purity and the extent of immune cell infiltration. These scores were derived using the ESTIMATE algorithm, which integrates gene expression data to estimate the proportion of stromal and immune cells in the tumor microenvironment. Correlations between *ATF5* expression and various immune cell subtypes were analyzed using Spearman's correlation. Immune cell subtypes included T follicular helper (Tfh) cells, CD8+ T cells, M1 macrophages, and regulatory T cells (Tregs). Additionally, the relationship between *ATF5* expression and immune checkpoint (ICP) molecules, such as PDCD1, CTLA4, and CD274, was evaluated. Tumor mutational burden (TMB) and neoantigen load were compared between high and low *ATF5* expression groups using Wilcoxon rank-sum tests. The MANTIS score, a measure of microsatellite instability (MSI), was also analyzed to assess its association with *ATF5* expression.

2.5 Single-cell transcriptomics analysis

To gain insights into the cellular heterogeneity and spatial distribution of *ATF5* expression, we analyzed single-cell RNA sequencing (scRNA-seq) data from the GSE168562 dataset using TISCH2 (https://academic.oup.com/nar/article/51/D1/D1425/6793806) [13]. The original study conducted by Li et al. employed cervical cancer and adjacent normal tissues that were obtained from a 53-year-old patient with HPV18-positive cervical squamous cell carcinoma who underwent surgical resection [14]. Uniform manifold approximation and projection (UMAP) clustering was performed to identify distinct cell populations within the tumor microenvironment, including malignant cells, stromal cells, and immune cells. Differential expression analysis was conducted to compare *ATF5* expression levels between normal and tumor tissues within each cell population. Specific attention was given to stromal cells, where *ATF5* expression was found to differ significantly between normal and tumor tissues. Subtypes of stromal cells, including endometrial stromal cells and smooth muscle cells (SMCs), were further analyzed to identify the primary contributors to this differential expression. Cell–cell

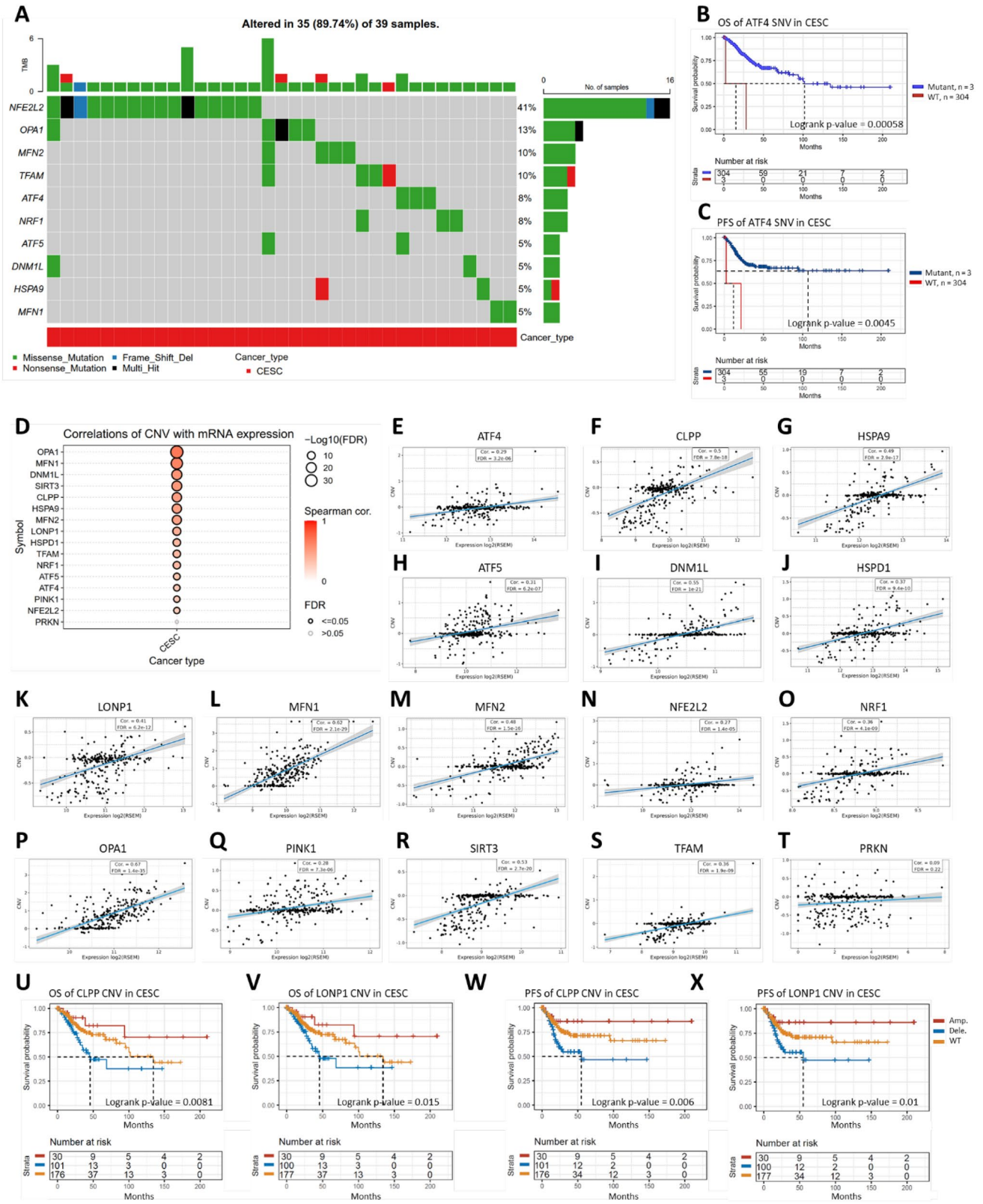
A
Altered in 35 (89.74%) of 39 samples.
TMB
No. of samples
NFE2L2 41%
OPA1 13%
MFN2 10%
TFAM 10%
ATF4 8%
NRF1 8%
ATF5 5%
DNM1L 5%
HSPA9 5%
MFN1 5%
Cancer_type
Missense_Mutation
Frame_Shift_Del
Nonsense_Mutation
Multi_Hit
CESC
B
OS of ATF4 SNV in CESC
Survival probability
Logrank p-value = 0.00058
Mutant, n = 3
WT, n = 304
Number at risk
Months
C
PFS of ATF4 SNV in CESC
Logrank p-value = 0.0045
D
Correlations of CNV with mRNA expression
−Log10(FDR)
Spearman cor.
FDR
<=0.05
>0.05
Symbol
Cancer type
E
ATF4
F
CLPP
G
HSPA9
H
ATF5
I
DNM1L
J
HSPD1
K
LONP1
L
MFN1
M
MFN2
N
NFE2L2
O
NRF1
P
OPA1
Q
PINK1
R
SIRT3
S
TFAM
T
PRKN
U
OS of CLPP CNV in CESC
Logrank p-value = 0.0081
V
OS of LONP1 CNV in CESC
Logrank p-value = 0.015
W
PFS of CLPP CNV in CESC
Logrank p-value = 0.006
X
PFS of LONP1 CNV in CESC
Logrank p-value = 0.01
Amp.
Dele.
WT

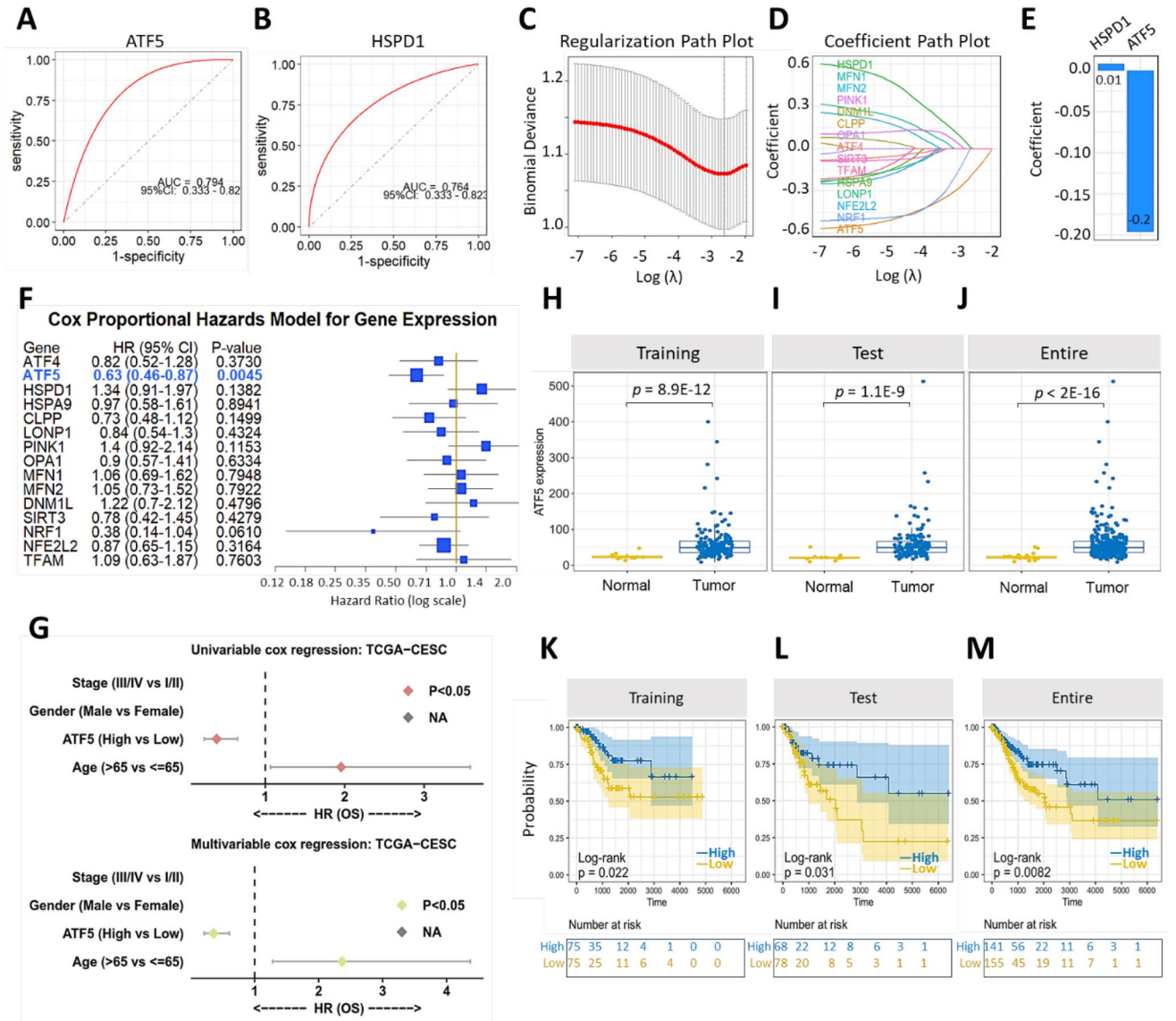

Fig. 3 Machine learning-driven analysis of UPR^{mt} genes reveals *ATF5*'s diagnostic and prognostic significance in CESC. **A**–**B** ROC curve analyzing the discriminatory power between normal tissue and tumor tissue for *ATF5* (**A**) and *HSPD1* (**B**). **C** Regularization path plot showing selection of the optimal regularization parameter (λ, lambda) for penalized regression model. **D** Coefficient path plot visualizing the change of each UPR^{mt} gene coefficient as lambda varies. Genes whose coefficients remain non-zero even at high lambda values are considered more relevant. **E** Bar chart showing coefficient values of most important genes. **F** Forest plot illustrating Cox hazard model that examines the effect of UPR^{mt} gene expression on the survival rate of the TCGA-CESC cohort. HR, hazard ratio. CI, confidence interval. **G** Forest plot illustrating univariable/multivariable Cox hazard model that examines the effect of *ATF5* on the survival rate of the TCGA-CESC cohort. HR, hazard ratio. OS, overall survival. **H**–**J** Box plot depicting *ATF5* expression levels in normal tissue and tumor tissue of the training group (**H**), test group (**I**) and entire group (**J**). **K**–**M** Kaplan–Meier plots of illustrating the overall survival probability of the training group (**K**), test group (**L**) and entire group (**M**), stratified by low and high *ATF5* expression levels, with a cutoff at the 55th percentile

interaction analysis was performed using the CellPhoneDB algorithm to identify key ligand-receptor pairs mediating interactions between stromal and malignant cells.

2.6 Gene set enrichment analysis (GSEA)

Gene set enrichment analysis (GSEA) was conducted to identify biological pathways associated with *ATF5* expression. Hallmark gene sets from the Molecular Signatures Database (MSigDB) were analyzed using the GENI platform (https://

www.sciencedirect.com/science/article/pii/S2001037023004105) [15]. Enrichment scores were calculated for each pathway, and pathways with significant positive correlations to specified gene expression were visualized.

2.7 Drug sensitivity analysis

Drug sensitivity data were retrieved from the Comprehensive Pancancer Analysis of Drug Sensitivity (CPADS) platform (https://smuonco.shinyapps.io/CPADS/) [16]. IC50 values were compared between high and low expression groups. Statistical significance was assessed using Wilcoxon rank-sum tests. To elucidate the mechanisms underlying drug sensitivity and resistance, we analyzed the mutational landscape between high and low *ATF5* expression groups using CAMOIP web server [12]. Additionally, the association between *ATF5* expression and key regulators of mitochondrial function was examined using its Expression module.

2.8 Artwork and visualization

All figures were created using BioRender (https://biorender.com/) and other visualization tools integrated into the respective analysis platforms. Data visualizations, including scatter plots, heatmaps, and survival curves, were generated using R and Python. Statistical analyses were performed using the "ggplot2" and "survminer" packages in R, ensuring high-quality and reproducible visualizations.

2.9 Statistical analysis

All statistical analyses were conducted using R (version 4.2.0) and Python (version 3.9). Survival analyses were performed using the Kaplan–Meier method, and log-rank tests were used to compare survival curves. Correlation analyses were conducted using Spearman's rank correlation. P-values less than 0.05 were considered statistically significant unless otherwise specified. For machine learning analyses, cross-validation was employed to ensure robustness and minimize overfitting.

3 Results

3.1 *Genetic profiling and clinical significance of UPR^{mt} genes in CESC*

We first analyzed genetic alterations of UPR^{mt} genes across CESC samples. *NFE2L2* was identified as the most frequently mutated UPR^{mt} gene, followed by *OPA1*, *MFN2*, *TFAM*, *ATF4*, *NRF1*, *ATF5*, *DNM1L*, *HSPA9*, and *MFN1* (Fig. 2A). Among these genes, only the *ATF4* mutant was associated with shorter overall survival time (Fig. 2B) and progression-free survival (Fig. 2C). Copy number variation (CNV) exhibited a positive correlation with mRNA expression levels across all UPR^{mt} genes (Fig. 2D–S), with the exception of *PRKN* (Fig. 2T). Deletions of *CLPP* and LONP1 were linked to shorter overall survival time (Fig. 2U and V) and progression-free survival (Fig. 2W and X).

3.2 *Machine learning-driven analysis of UPR^{mt} genes reveals ATF5's diagnostic and prognostic significance*

ROC analysis unveiled the discriminatory performance of UPR^{mt} genes, ranging from acceptable to excellent in distinguishing normal tissue from tumor tissue, including *ATF4* (Supplementary Fig. S1A), *ATF5* (Fig. 3A), *HSPD1* (Fig. 3B), *TFAM* (Supplementary Fig. S1B), *LONP1* (Supplementary Fig. S1C), *PINK1* (Supplementary Fig. S1D), *OPA1* (Supplementary Fig. S1E), and *MFN1* (Supplementary Fig. S1F), as well as those with poor discriminatory ability, such as *HSPA9* (Supplementary Fig. S1G), *CLPP* (Supplementary Fig. S1H), *DNM1L* (Supplementary Fig. S1I), *SIRT3* (Supplementary Fig. S1J), *NRF1* (Supplementary Fig. S1K), *NFE2L2* (Supplementary Fig. S1L), and *MFN2* (Supplementary Fig. S1M).

To select the most impactful genes for predicting patient outcomes, we utilized the LASSO machine learning algorithm to identify most relevant genes for survival prediction. This approach determined the optimal level of regularization (Fig. 3C), revealed genes that remained significant at this regularization level (Fig. 3D), and yielded coefficients for the two most relevant genes: *HSPD1* and *ATF5* (Fig. 3E). Subsequently, we utilized a Cox regression model to evaluate the impact of UPR^{mt} genes, identifying *ATF5* expression levels as an independent prognostic factor for overall survival time in CESC patients (Fig. 3F). Notably, *ATF5* expression levels also remained an independent prognostic factor even after adjusting

Fig. 4 Impact of *ATF5* expression on the shaping of tumor-immune microenvironment and immunogenicity. **A**, **B** and **G** Heatmap illustrating the Spearman correlation results of *ATF5* expression with immune scores (**A**), immune cell infiltrate (**B**) and immunoinhibitors (**G**) across pan-cancer types. CESC cohort highlighted with green boxes. Hash sign (#) indicating immune checkpoint genes. $*p < 0.05$, $**p < 0.01$. **C**–**F** Scatter plots exhibiting correlation analysis of *ATF5* with representative marker of Tfh (*ICOS*) (**C**), CD8 T-cell (*CD8A*) (**D**), Treg (*FOXP3*) (**E**), macrophage M1 (*NOS2*) (**F**). **H**–**O** Scatter plots exhibiting correlation analysis of *ATF5* with immune checkpoint genes *LAG3* (**H**), *HAVCR2* (**I**), *TIGIT* (**J**), *BTLA* (**K**), *PDCD1* (**L**), *CTLA4* (**M**), *CD274* (**N**) and *CD96* (**O**). **P**–**R** Box plots showing impact of high vs. low expression of *ATF5* on tumor mutation burden (TMB) (**P**), neoantigen load (**Q**) and Microsatellite Analysis for Normal-Tumor Instability (MANTIS) score (**R**). $*p < 0.05$ between two groups using the Mann–Whitney U test

for age (Fig. 3G). CESC tumor exhibited higher *ATF5* expression compared to normal tissues in the training (Fig. 3H), test (Fig. 3I) and entire TCGA datasets (Fig. 3J). This finding was further corroborated by immunohistochemistry data from the Human Protein Atlas, which demonstrated consistent protein-level ATF5 overexpression patterns (Supplementary Fig. S2). Elevated *ATF5* expression was associated with longer overall survival time in the training (Fig. 3K), test (Fig. 3L) and entire TCGA datasets (Fig. 3M).

3.3 Potential connection between ATF5 expression and therapeutic response

To investigate the mechanistic relationship between *ATF5* dependency and biological pathways, along with cellular response to chemotherapy, we analyzed genome-wide CRISPR screening data available in the DepMap Portal (Supplementary Fig. S3A). Analysis revealed that CRISPR-mediated knockout of *ATF5* (indicated by more negative Gene Effect scores) showed significant negative correlations with WikiPathways terms: "cellular proteostasis" (Supplementary Figure S3B) and "receptor-mediated mitophagy" (Supplementary Fig. S3C) in CESC cell lines, as defined by. These findings suggest that *ATF5* plays a crucial role in activating both proteostasis and mitophagy pathways. Furthermore, *ATF5* Gene Effect scores negatively correlated with CESC cellular sensitivity to fluorouracil (Supplementary Figure S3D and E), an FDA-approved chemotherapeutic agent for CESC treatment. This observation suggests that loss of *ATF5* function in CESC cells may contribute to fluorouracil resistance in CESC cells, establishing a potential connection between ATF5 expression and therapeutic response.

3.4 Impact of ATF5 on tumor-immune microenvironment and immunogenicity

To investigate the immuno-oncological role of *ATF5*, we analyzed its association with key characteristics of the tumor-immune microenvironment. In CESC cohort, *ATF5* expression levels correlated positively with the Stromal Score, Immune Score and ESTIMATE score, indicating that *ATF5* expression is linked to a higher proportion of stromal content, increased immune cell infiltration, and reduced tumor purity, respectively (Fig. 4A). Further analysis revealed distinct correlations between *ATF5* expression and various immune cell subtypes (Fig. 4B). Notably, *ATF5* expression showed significant positive correlation with anti-tumoral cells, including T follicular helper (Tfh) cells (Fig. 4C), CD8 T cells (Fig. 4D), and M1 macrophages (Fig. 4E), while also exhibiting a positive correlation with pro-tumoral regulatory T cells (Treg) (Fig. 4F). Importantly, *ATF5* expression levels presented a positive correlation with most immunoinhibitors (Fig. 4G). Among these genes, *ATF5* expression levels strongly correlated with immune checkpoints (ICP) molecules, including LAG3 (Fig. 4H), HAVCR2 (Fig. 4I), TIGIT (Fig. 4J), PDCD1 (Fig. 4K), CTLA4 (Fig. 4L), CD274 (Fig. 4M), BTLA (Fig. 4N) and CD96 (Fig. 4O), suggesting a potential role in ICP regulation. In addition, patients with high *ATF5* expression levels presented elevated levels of TMB (Fig. 4P) and neoantigen load (Fig. 4Q), while showing no significant difference in MANTIS Score (Fig. 4R), compared to those with low *ATF5* expression. These findings suggest that high *ATF5* expression is associated with an immunologically active tumor microenvironment, characterized by increased immune cell infiltration. The elevated ICP expression and higher mutational burden in population with high *ATF5* expression potentially indicate favorable conditions for immunotherapy.

3.5 Single-cell transcriptomics reveals ATF5 distribution, cellular heterogeneity and cell–cell interaction

To further elucidate the cellular heterogeneity and complex interactions underlying *ATF5*'s role in CESC, we retrieved single-cell RNA sequencing (scRNA-seq) analysis from GSE168562. This comprehensive approach allowed us to map the distribution of *ATF5* expression across different cell populations within the tumor microenvironment and decipher the intricate cell–cell communication networks that may influence disease progression. Building upon our previous observations regarding *ATF5*'s association with stromal content, immune cell infiltration and ICP regulation, this single-cell

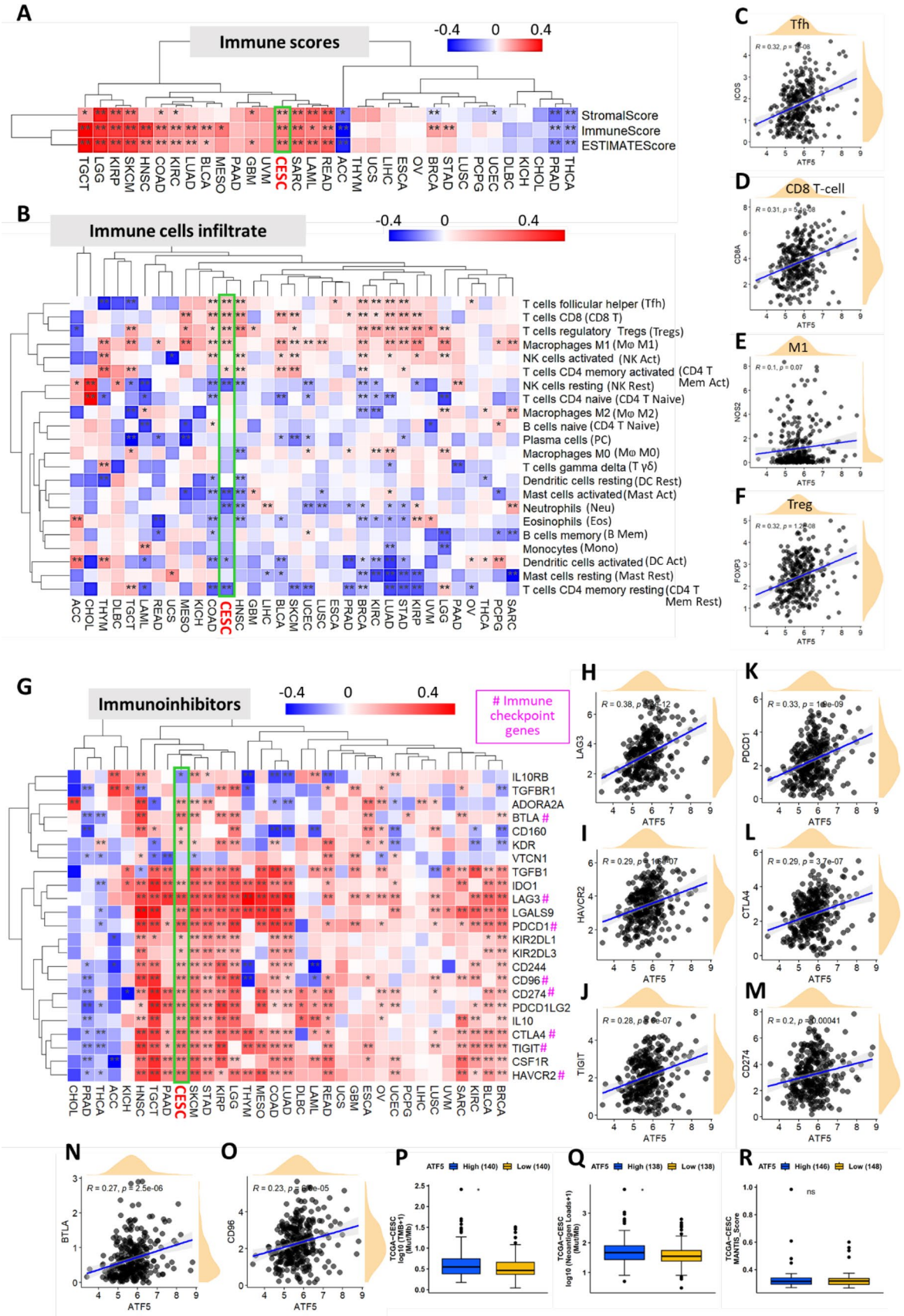
A
Immune scores
-0.4 0 0.4
StromalScore
ImmuneScore
ESTIMATEScore
TGCT LGG KIRP SKCM HNSC COAD KIRC LUAD BLCA MESO PAAD GBM UVM CESC SARC LAML READ ACC THYM UCS LIHC ESCA OV BRCA STAD LUSC PCPG UCEC DLBC KICH CHOL PRAD THCA
B
Immune cells infiltrate
-0.4 0 0.4
T cells follicular helper (Tfh)
T cells CD8 (CD8 T)
T cells regulatory Tregs (Tregs)
Macrophages M1 (Mφ M1)
NK cells activated (NK Act)
T cells CD4 memory activated (CD4 T Mem Act)
NK cells resting (NK Rest)
T cells CD4 naive (CD4 T Naive)
Macrophages M2 (Mφ M2)
B cells naive (CD4 T Naive)
Plasma cells (PC)
Macrophages M0 (Mφ M0)
T cells gamma delta (T γδ)
Dendritic cells resting (DC Rest)
Mast cells activated (Mast Act)
Neutrophils (Neu)
Eosinophils (Eos)
B cells memory (B Mem)
Monocytes (Mono)
Dendritic cells activated (DC Act)
Mast cells resting (Mast Rest)
T cells CD4 memory resting (CD4 T Mem Rest)
ACC CHOL THYM DLBC TGCT LAML READ UCS MESO KICH COAD CESC HNSC GBM LIHC BLCA SKCM UCEC LUSC ESCA PRAD BRCA KIRC LUAD STAD KIRP UVM LGG PAAD OV THCA PCPG SARC
C
Tfh
ICOS
ATF5
D
CD8 T-cell
CD8A
ATF5
E
M1
NOS2
ATF5
F
Treg
FOXP3
ATF5
G
Immunoinhibitors
-0.4 0 0.4
Immune checkpoint genes
IL10RB
TGFBR1
ADORA2A
BTLA #
CD160
KDR
VTCN1
TGFB1
IDO1
LAG3 #
LGALS9
PDCD1 #
KIR2DL1
KIR2DL3
CD244
CD96 #
CD274 #
PDCD1LG2
IL10
CTLA4 #
TIGIT #
CSF1R
HAVCR2 #
CHOL PRAD THCA ACC KICH HNSC TGCT PAAD CESC SKCM STAD KIRP LGG THYM MESO COAD LUAD DLBC LAML READ UCS GBM ESCA OV UCEC PCPG LIHC LUSC UVM SARC KIRC BLCA BRCA
H
LAG3
ATF5
K
PDCD1
ATF5
I
HAVCR2
ATF5
L
CTLA4
ATF5
J
TIGIT
ATF5
M
CD274
ATF5
N
BTLA
ATF5
O
CD96
ATF5
P
ATF5 High (140) Low (140)
TCGA-CESC log10 (Neoantigen Loads+1) (Mut/Mb)
Q
ATF5 High (138) Low (138)
TCGA-CESC log10 (Neoantigen Loads+1) (Mut/Mb)
R
ATF5 High (146) Low (148)
ns
TCGA-CESC MANTIS_Score

Fig. 5 Single-cell transcriptomics reveals cellular heterogeneity and *ATF5* distribution in CESC dataset of GSE168652. **A** Pie chart displaying cell type statistics of dataset. **B**–**D** Uniform Manifold Approximation and Projection (UMAP) plots exhibiting cell type deconvolution of malignancy (**B**) and major-lineage (**C**) and cellular distribution of *ATF5* expression (**D**). **E**–**F** Violin plot demonstrating *ATF5* expression levels of normal vs. tumor in various cell sub-populations

resolution analysis provides deeper insights into the spatial and functional organization of *ATF5*-expressing cells within the tumor ecosystem.

Using uniform manifold approximation and projection (UMAP) clustering analysis (Fig. 5A and B), we identified that malignant cells represented the most abundant population, followed by stromal cells and immune cells (Fig. 5C), with *ATF5* expression showing uniform distribution among these cell populations (Fig. 5D). Notably, *ATF5* showed differential expression between normal and tumor tissue in stromal cells, but not in other cell populations (Fig. 5E). Further analysis revealed that this *ATF5* differential expression in stromal cells was predominantly attributed to changes in endometrial stromal cells and smooth muscle cells (SMC), while remaining unchanged in endothelial cells and fibroblasts (Fig. 5F).

The Cell–Cell Interaction analysis uncovered prominent interaction counts between endometrial stromal cells and malignant cells (Fig. 6A and B). Most notably, we identified key cell surface molecules mediating these interactions, including COL6A1–CD44, COL6A2–CD44, COL6A3–CD44, FN1–CD44 and THBS1–CD47 (Fig. 6C).

3.6 ATF5 expression is associated with P-stalk ribosome-mediated immune response regulation

To gain more insights into the underlying mechanisms, we conducted gene set enrichment analysis (GSEA). Figure 7A summarizes the upregulated Hallmark gene sets wherein genes positively correlated with ATF5 are significantly enriched, with notably robust enrichment in interferon gamma (IFNγ) response (Fig. 7B), interferon alpha (IFNα) response (Fig. 7C) and oxidative phosphorylation (Fig. 7D).

Recent studies have demonstrated that IFNγ/IFNα exposure leads to the formation of specialized P-stalk ribosomes (PSR), which play a critical role in orchestrating immune surveillance [17]. These PSR engage in selective translation of immune response proteins within the endoplasmic reticulum (ER), including those involved in antigen processing and presentation pathways essential for cytotoxic T cell activation. Furthermore, the PSR have been shown to facilitate the modulation of T cell-mediated responses by dynamically association with specific ribosomal cofactors and molecular complexes that regulate cytokine signaling and the synthesis of major histocompatibility complex (MHC) proteins, thereby enhancing the immune system's ability to detect and eliminate abnormal or cancerous cells. The mechanistic insights provided by these findings suggest that P-stalk ribosomes act as key regulators of immune surveillance at the interface of translation and immune signaling. To explore this mechanism further, we subsequently investigated the *ATF5*–PSR relationship in CESC. Our analysis revealed that *ATF5* positively correlated with key PSR-constituent genes, including *RPLP0* (Fig. 7E), *RPLP1* (Fig. 7F) and *RPLP2* (Fig. 7G). Furthermore, in a comprehensive analysis of *ATF5* expression levels with MHC molecules (Fig. 7H), we observed significant positive correlations between *ATF5* expression levels and critical molecules governing antigen-presenting and immunosurveillance: *B2M* (Fig. 7I), *HLA-A* (Fig. 7J), *HLA-B* (Fig. 7K), *HLA-C* (Fig. 7L), *TAP1* (Fig. 7M), *TAP2* (Fig. 7N), *TAPBP* (Fig. 7O). The proposed mechanism underlying *ATF5*-PSR-mediating immune response is depicted in Fig. 7P.

3.7 Therapeutic compound sensitivity associated with ATF5 expression patterns

In light of our comprehensive characterization of *ATF5*'s role in outcome prediction and immune regulation, we sought to identify potential therapeutic compounds that could modulate *ATF5*-associated pathways. Computational drug sensitivity analysis using CPADS revealed that CESC cells with low *ATF5* expression demonstrated significantly higher IC50 values in response to cisplatin (Fig. 8A), paclitaxel (Fig. 8B), and etoposide (Fig. 8C), indicating acquired chemoresistance. Conversely, these cells showed enhanced sensitivity to imatinib, as evidenced by significantly lower IC50 values (Fig. 8D).

Given that DNA damage response is the primary therapeutic mechanism for cisplatin, paclitaxel and etoposide, we examined the relationship between *ATF5* expression and mutations in cancer-associated genes. Our analysis revealed that low *ATF5* expression levels correlate with reduced mutational frequency of *EP300* compared to high *ATF5* expression levels (Fig. 8E). This finding is particularly relevant as functional *EP300* plays a crucial role in DNA repair and cancer cell survival [18], suggesting that *ATF5* downregulation may contribute to chemoresistance through *EP300*-dependent mechanisms.

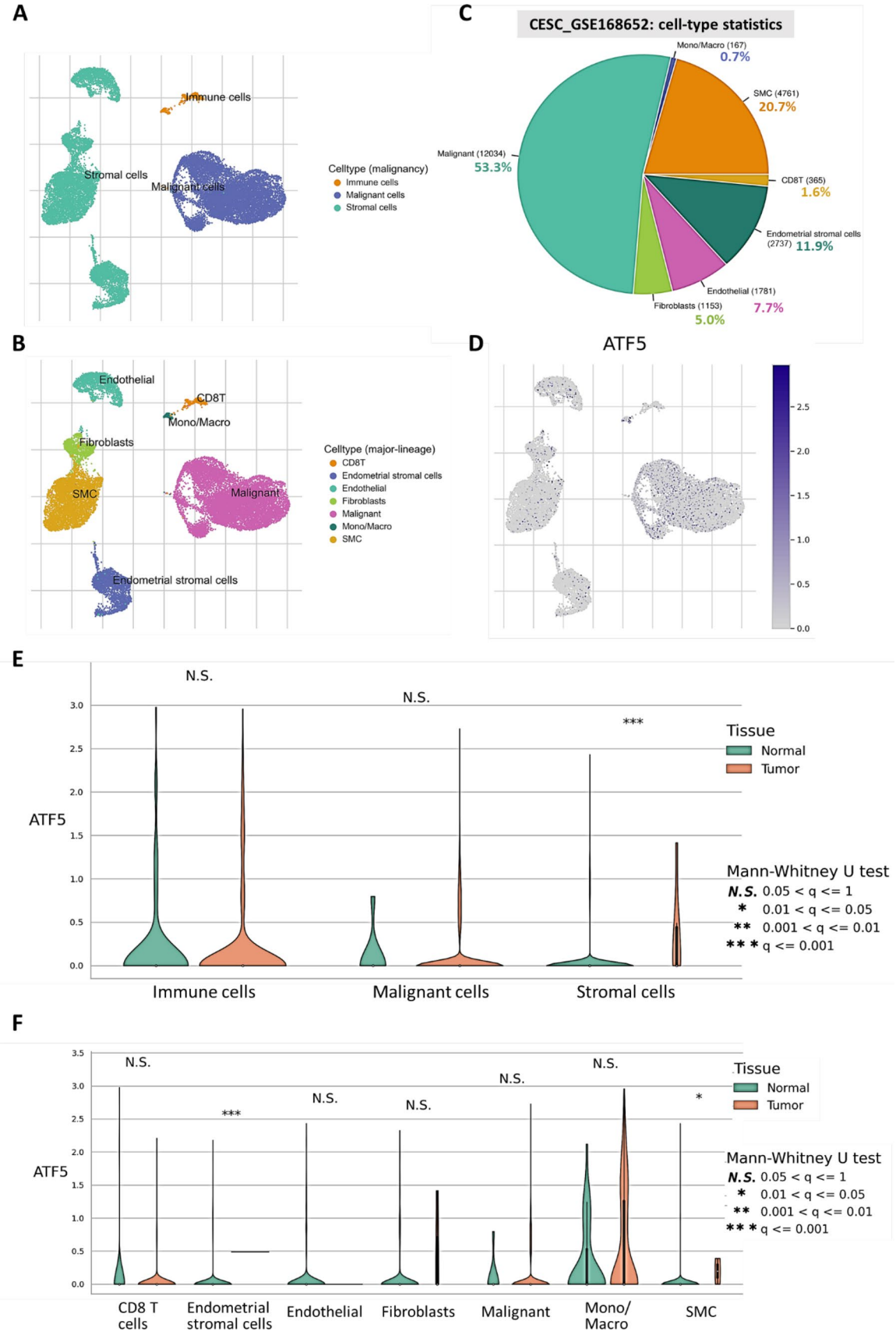
A
Immune cells
Stromal cells
Malignant cells
Celltype (malignancy)
Immune cells
Malignant cells
Stromal cells
C
CESC_GSE168652: cell-type statistics
Mono/Macro (167)
0.7%
SMC (4761)
20.7%
Malignant (12034)
53.3%
CD8T (365)
1.6%
Endometrial stromal cells
(2737) 11.9%
Endothelial (1781)
7.7%
Fibroblasts (1153)
5.0%
B
Endothelial
CD8T
Mono/Macro
Fibroblasts
SMC
Malignant
Endometrial stromal cells
Celltype (major-lineage)
CD8T
Endometrial stromal cells
Endothelial
Fibroblasts
Malignant
Mono/Macro
SMC
D
ATF5
2.5
2.0
1.5
1.0
0.5
0.0
E
N.S.
N.S.
***
ATF5
Tissue
Normal
Tumor
Mann-Whitney U test
N.S. 0.05 < q <= 1
* 0.01 < q <= 0.05
** 0.001 < q <= 0.01
*** q <= 0.001
Immune cells
Malignant cells
Stromal cells
F
N.S.
***
N.S.
N.S.
N.S.
N.S.
*
ATF5
Tissue
Normal
Tumor
Mann-Whitney U test
N.S. 0.05 < q <= 1
* 0.01 < q <= 0.05
** 0.001 < q <= 0.01
*** q <= 0.001
CD8 T cells
Endometrial stromal cells
Endothelial
Fibroblasts
Malignant
Mono/ Macro
SMC

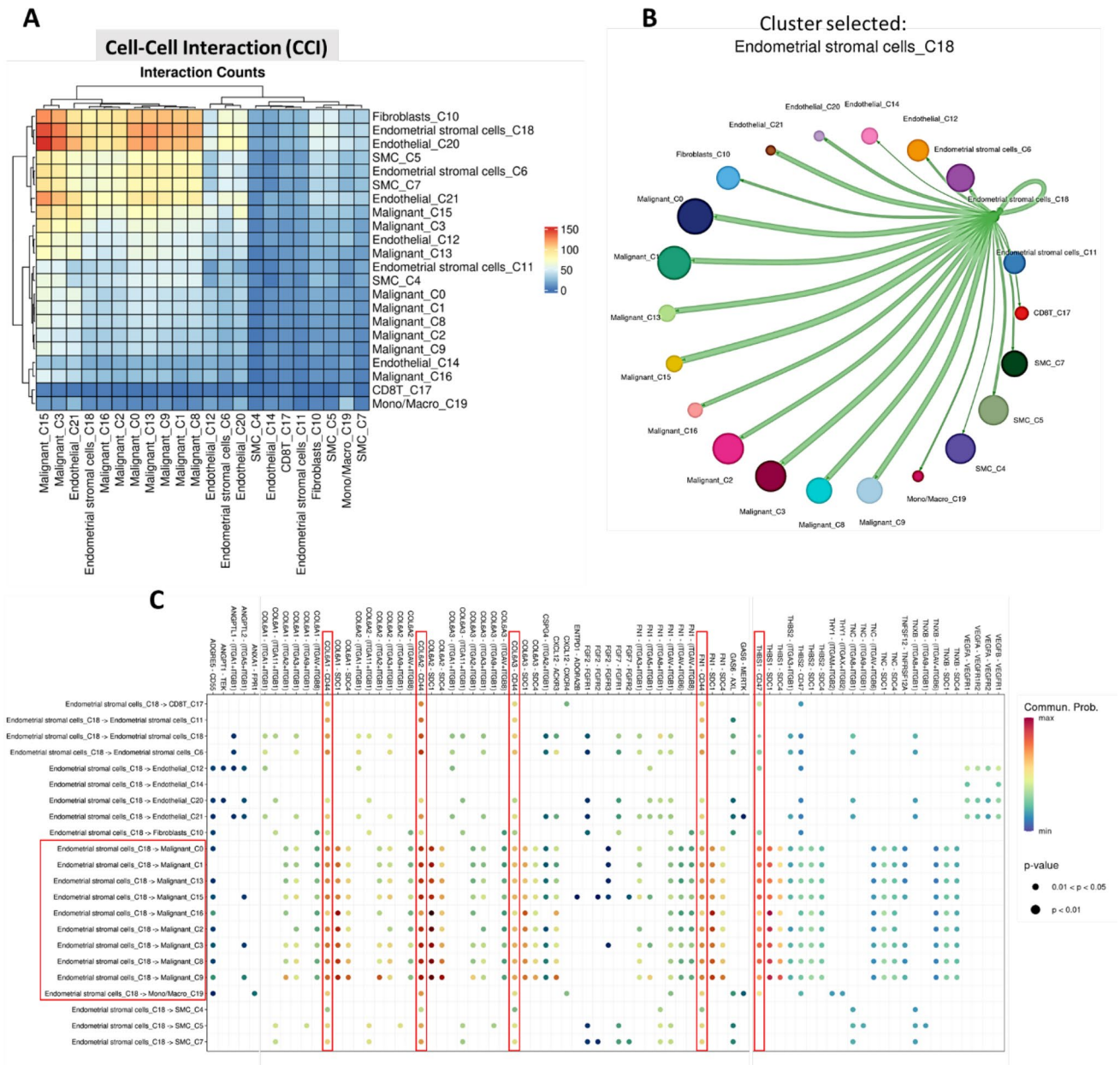

Fig. 6 Single-cell transcriptomics unveils cell–cell interaction in CESC sample. **A**, **B** Cell–cell interaction (CCI) illustrated using heatmap (**A**) and interaction network (**B**). **A** Heatmap illustrating cell–cell interaction (CCI) through interaction counts between cell clusters. **B** Network illustrating interaction of selected cluster (Endometrial stromal cells_C18) with other clusters. **C** Dot plot showing communication probability of ligand-receptor in specific cell–cell interaction

Previous research has established that mitochondrial inhibition enhances imatinib's anti-tumor efficacy [19]. Therefore, we examined the relationship between *ATF5* expression and key regulators of mitochondrial function. Our results demonstrated that low *ATF5* expression levels are associations with downregulation of several critical mitochondrial regulators, including *ATF4* (Fig. 8F), *NRF1* (Fig. 8G), *CLPP* (Fig. 8H), *HSPD1* (Fig. 8I), *HSPE1* (Fig. 8J), *GPX1* (Fig. 8K), *GPX4* (Fig. 8L) and *SOD1* (Fig. 8M). Figure 8N presents an integrated model illustrating the impact of *ATF5* expression on drug sensitivity and its underlying molecular mechanisms.

4 Discussion

In this comprehensive study, we leveraged advanced machine learning algorithms to unravel the complex role of UPR^{mt} in CESC, demonstrating the power of computational approaches in identifying clinically relevant molecular patterns. Our integrated analysis, summarized in a comprehensive schematic representation (Fig. 9), reveals *ATF5* as a central orchestrator bridging clinical outcomes with fundamental mitochondrial-nuclear communication in CESC.

Specifically, our LASSO-based feature selection and Cox regression modeling, combined with multi-omics analyses, led to several novel findings. First, our systematic machine learning approach successfully filtered through multiple UPR^{mt} components to identify *ATF5* as the most significant prognostic factor in CESC, highlighting the advantage of unbiased computational methods over traditional single-gene analyses. Second, we uncovered *ATF5*'s significant role in modulating the tumor immune microenvironment, particularly through its association with immune cell infiltration and checkpoint regulation. Third, our single-cell analysis revealed cell-type specific patterns of *ATF5* expression and identified crucial stromal-tumor cell interactions. Fourth, we discovered a potential mechanism involving PSR in mediating *ATF5*'s immunomodulatory effects. Finally, we demonstrated *ATF5*'s association with treatment responses to various therapeutic compounds. This machine learning-driven approach not only enhanced the robustness of our findings but also provided a framework for similar analyses in other cancer types.

The identification of *ATF5* as a favorable prognostic marker in CESC contrasts with its reported oncogenic role in other cancers [20–22]. This discrepancy might be explained by our finding that *ATF5* expression correlates with enhanced immune surveillance and increased immune cell infiltration in CESC. The positive correlation between *ATF5* expression and anti-tumoral immune cells, including CD8 T cells and M1 macrophages, suggests that *ATF5* might contribute to an immunologically "hot" tumor microenvironment. This is further supported by the association between high *ATF5* expression and elevated TMB, factors known to enhance tumor immunogenicity [23].

ATF5, as a critical regulator in the UPR^{mt} pathway, exhibits tumor-suppressive effects in CESC through various mechanisms. Firstly, our findings indicate that *ATF5* expression is associated with an immunologically active tumor microenvironment. Specifically, high ATF5 expression correlates with increased immune cell infiltration, elevated immune checkpoint expression, and higher tumor mutational burden. This suggests that *ATF5* may promote anti-tumor immune activity, which could partially explain its tumor-suppressive role in CESC. In addition, pathway enrichment analysis revealed that *ATF5* is involved in PSR-mediated immune response regulation. This unique pathway involvement could reflect tissue-specific mitochondrial signaling dynamics that impact the immune interactions in CESC more strongly than in other cancers. Furthermore, single-cell RNA sequencing data demonstrated distinct expression patterns of *ATF5* in stromal cells, particularly in endometrial stromal and smooth muscle cells. This cellular context may influence *ATF5*'s interactions with other components of the tumor microenvironment, driving its tumor-suppressive effects in a manner specific to cervical tissue. Finally, *ATF5* appears to influence treatment responses in CESC. Drug sensitivity analysis revealed that low *ATF5* expression is associated with resistance to traditional chemotherapeutics (e.g., cisplatin, paclitaxel, etoposide). Conversely, high ATF5 expression may sensitize cancer cells to these treatments while also activating alternative response mechanisms, such as *EP300*-dependent pathways. These findings collectively highlight the potential tissue-specific roles of *ATF5*, including its interactions with mitochondrial signaling pathways, immune modulation, and effects on treatment sensitivity.

Our single-cell RNA sequencing analysis revealed that *ATF5*'s differential expression between normal and tumor tissues was primarily observed in stromal cells, particularly in endometrial stromal cells and SMCs. The identified interactions between these stromal cells and malignant cells, mediated through specific ligand-receptor pairs, suggest a complex interplay that may influence tumor progression and immune responses. This finding adds to the growing recognition of stromal cells as key regulators of the tumor microenvironment [24–27].

Perhaps the most intriguing finding is the potential mechanism involving PSR. The strong correlation between *ATF5* expression and PSR-constituent genes, coupled with enrichment in interferon response pathways, suggests that *ATF5* might regulate immune responses through PSR-mediated protein translation. This mechanism could explain the observed associations with MHC molecules and antigen-presenting machinery, providing a novel link between mitochondrial stress responses and immune regulation in cancer.

The differential drug sensitivity patterns associated with *ATF5* expression levels have important clinical implications. The observation that low *ATF5* expression correlates with resistance to conventional chemotherapeutics while conferring sensitivity to imatinib suggests potential strategies for personalized treatment approaches. The association between

Fig. 7 Involvement of *ATF5* in cytokine response and P-stalk ribosome-conferred immunosurveillance. **A** Bubble plot summarizing significantly upregulated Hallmark gene sets associated with genes positively correlated with *ATF5*. **B**–**D** GESA plots showing normalized enrichment score (NES), family-wise error rate (FWER), false discovery rate (FDR) of gene set "INTERFERON GAMMA RESPONSE" (**B**), "INTERFERON ALPHA RESPONSE" (**C**) and "OXIDATIVE PHOSPHORYLATION" (**D**). **E**–**G** Scatter plots illustrating correlation of *ATF5* with representative markers of P-stalk ribosome, RPLP0 (**E**), RPLP1 (**F**) and RPLP2 (**G**). **H** Heatmap depicting correlation between ATF5 expression and MHC molecules across pan cancers. CESC highlighted by green box. **I**–**O** Scatter plots illustrating correlation of *ATF5* expression with B2M (**I**), HLA-A (**J**), HLA-B (**K**), *HLA-C* (**L**), *TAP1* (**M**), *TAP2* (**N**), and *TAPBP* (**O**). **P** Proposed model illustrating possible involvement of *ATF5* in interferon gamma/alpha response and P-stalk ribosome elements, which act to translate transmembrane domains of receptor molecules, ultimately promoting Immunosurveillance

ATF5 expression and *EP300* mutations, along with various mitochondrial regulators, provides mechanistic insights into these differential treatment responses.

EP300, as a transcriptional coactivator with histone acetyltransferase activity, plays a key role in maintaining genomic stability and regulating DNA damage responses. Mutations or functional alterations in *EP300* can impair DNA repair mechanisms, particularly those involved in homologous recombination and nucleotide excision repair. Such defects may lead to the accumulation of genomic instability, contributing to resistance against conventional DNA-damaging chemotherapeutics such as cisplatin, paclitaxel, and etoposide. Our analysis suggests that *ATF5* expression may influence the functional interplay between *EP300* and DNA repair pathways. For example, low *ATF5* expression, which correlates with increased chemoresistance, might exacerbate the effects of *EP300* mutations by further diminishing DNA repair capacity. Conversely, high ATF5 expression could counterbalance the negative effects of *EP300* mutations by enhancing mitochondrial proteostasis and stress signaling pathways, potentially restoring some aspects of genomic stability and improving susceptibility to chemotherapy. In light of these findings, supplementing *EP300* mutations with high *ATF5* expression may provide a novel strategy to address DNA repair defects and combat chemoresistance. This interplay underscores the potential therapeutic value of targeting *ATF5*-related pathways in conjunction with *EP300* mutations to improve treatment efficacy in CESC patients.

Several limitations of our study should be acknowledged. First, while our computational analyses suggest multiple mechanisms, experimental validation is needed to confirm these findings. Second, the temporal dynamics of *ATF5*-mediated responses and their relationship with disease progression require further investigation. Third, the potential therapeutic strategies suggested by our findings need clinical validation.

The single-cell RNA sequencing findings are based on the GSE168562 dataset, which represents a limited sample size typical of many scRNA-seq studies. As such, these observations should be interpreted as preliminary evidence rather than definitive proof of stromal-specific *ATF5* expression patterns. The cell-type specific differences we observed, though intriguing, would benefit from validation in larger cohorts and through complementary experimental approaches. Despite these limitations, our analysis provides valuable initial insights that can guide future investigations into the role of *ATF5* in stromal cell populations. Further studies with expanded sample sizes will be crucial for confirming these preliminary findings and establishing their broader biological significance. In addition, our analysis uncovered significant cell–cell interactions, including COL6A1-CD44; however, their mechanistic relationship to *ATF5* or UPR^{mt} pathways remains to be elucidated. Nevertheless, these findings provide valuable insights into the broader changes in cellular communication within the tumor microenvironment that occur concurrent with *ATF5*-mediated alterations. The identified interaction patterns may serve as important molecular signatures that represent downstream effects of *ATF5* regulation or parallel pathways that contribute to the overall tumor phenotype. Future studies investigating the potential indirect connections between *ATF5* and these communication networks could reveal novel regulatory mechanisms and therapeutic targets. Moreover, examining how *ATF5*-mediated stress responses might influence the expression of these ligand-receptor pairs could uncover previously unknown aspects of tumor cell adaptation and survival.

While our study reveals significant correlations between *ATF5* and various molecular features in CESC, we acknowledge the limitations in establishing direct causality. The observed associations of *ATF5* with immune checkpoint expression and *EP300* mutations provide valuable insights into potential regulatory networks, but require further experimental validation. The correlation between *ATF5* and immune checkpoints suggests its possible role in tumor immune regulation, supported by previous studies showing *ATF5*'s involvement in cellular stress responses and survival pathways [2]. Similarly, the association with *EP300* mutations is particularly intriguing given *EP300*'s established role as a histone acetyltransferase and transcriptional co-activator [28]. *EP300* has been shown to regulate various stress-response pathways, potentially intersecting with *ATF5*'s functions. These correlative findings, while preliminary, establish a foundation for future mechanistic studies. Further experimental approaches, such as ChIP-seq analysis, protein–protein interaction

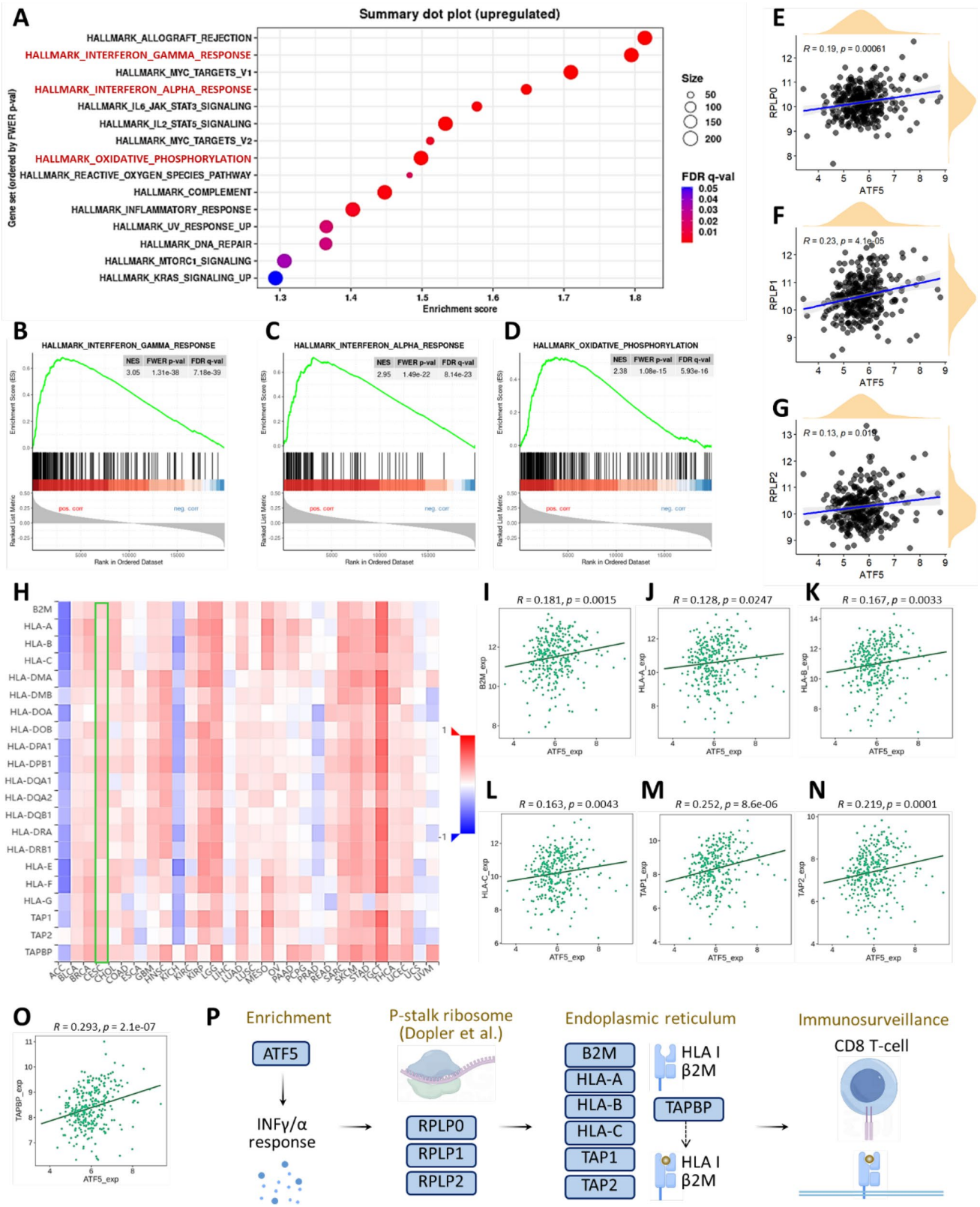
A
Summary dot plot (upregulated)
HALLMARK_ALLOGRAFT_REJECTION
HALLMARK_INTERFERON_GAMMA_RESPONSE
HALLMARK_MYC_TARGETS_V1
HALLMARK_INTERFERON_ALPHA_RESPONSE
HALLMARK_IL6_JAK_STAT3_SIGNALING
HALLMARK_IL2_STAT5_SIGNALING
HALLMARK_MYC_TARGETS_V2
HALLMARK_OXIDATIVE_PHOSPHORYLATION
HALLMARK_REACTIVE_OXYGEN_SPECIES_PATHWAY
HALLMARK_COMPLEMENT
HALLMARK_INFLAMMATORY_RESPONSE
HALLMARK_UV_RESPONSE_UP
HALLMARK_DNA_REPAIR
HALLMARK_MTORC1_SIGNALING
HALLMARK_KRAS_SIGNALING_UP
Gene set (ordered by FWER p-val)
Enrichment score
Size
FDR q-val
B
HALLMARK_INTERFERON_GAMMA_RESPONSE
C
HALLMARK_INTERFERON_ALPHA_RESPONSE
D
HALLMARK_OXIDATIVE_PHOSPHORYLATION
E
R = 0.19, p = 0.00061
RPLP0
ATF5
F
R = 0.23, p = 4.1e-05
RPLP1
ATF5
G
R = 0.13, p = 0.019
RPLP2
ATF5
H
B2M
HLA-A
HLA-B
HLA-C
HLA-DMA
HLA-DMB
HLA-DOA
HLA-DOB
HLA-DPA1
HLA-DPB1
HLA-DQA1
HLA-DQA2
HLA-DQB1
HLA-DRA
HLA-DRB1
HLA-E
HLA-F
HLA-G
TAP1
TAP2
TAPBP
I
R = 0.181, p = 0.0015
B2M_exp
ATF5_exp
J
R = 0.128, p = 0.0247
HLA-A_exp
ATF5_exp
K
R = 0.167, p = 0.0033
HLA-B_exp
ATF5_exp
L
R = 0.163, p = 0.0043
HLA-C_exp
ATF5_exp
M
R = 0.252, p = 8.6e-06
TAP1_exp
ATF5_exp
N
R = 0.219, p = 0.0001
TAP2_exp
ATF5_exp
O
R = 0.293, p = 2.1e-07
TAPBP_exp
ATF5_exp
P
Enrichment
ATF5
INFγ/α response
P-stalk ribosome (Dopler et al.)
RPLP0
RPLP1
RPLP2
Endoplasmic reticulum
B2M
HLA-A
HLA-B
HLA-C
TAP1
TAP2
HLA I β2M
TAPBP
HLA I β2M
Immunosurveillance
CD8 T-cell

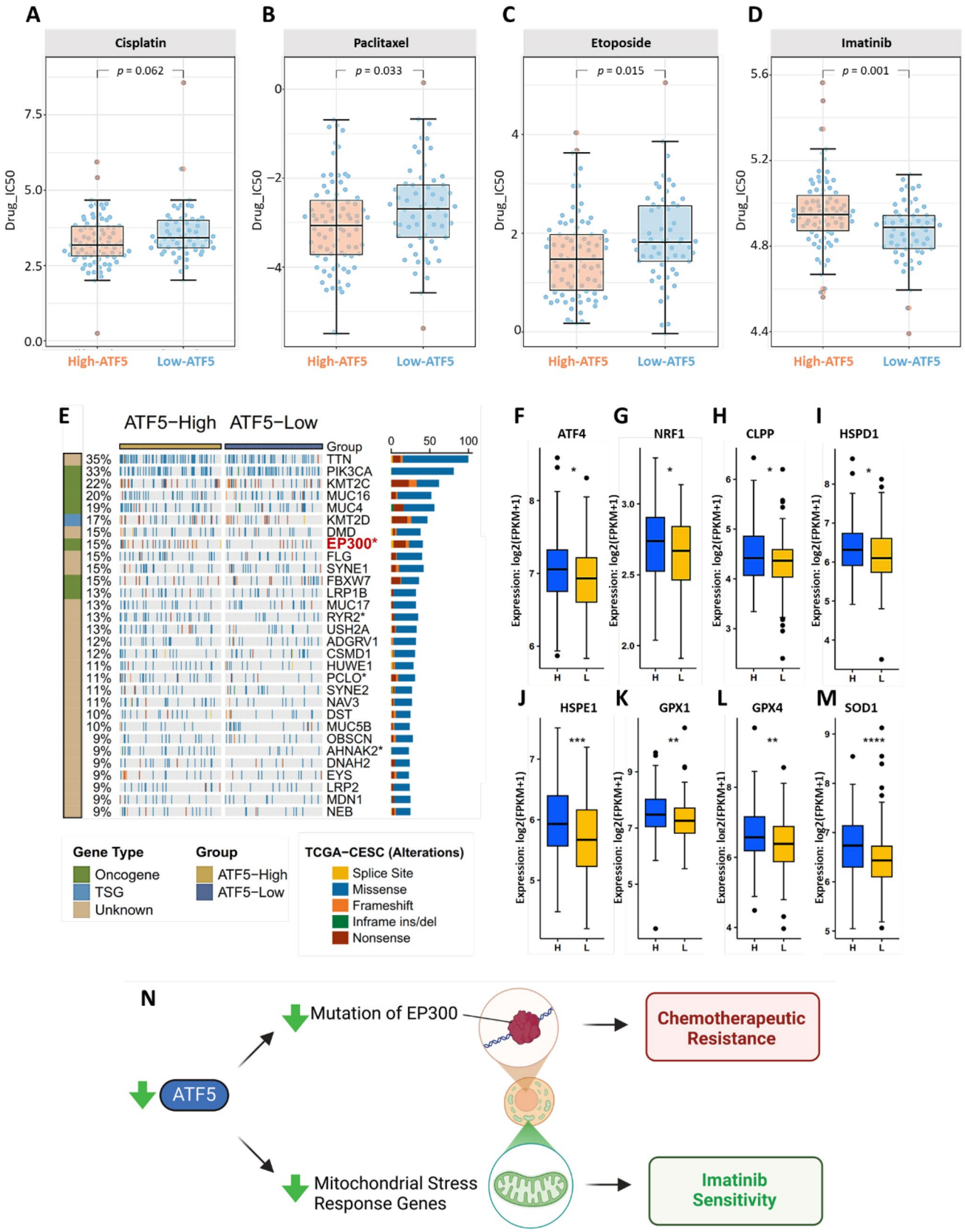
A
Cisplatin
p = 0.062
Drug_IC50
High-ATF5
Low-ATF5
B
Paclitaxel
p = 0.033
C
Etoposide
p = 0.015
D
Imatinib
p = 0.001
E
ATF5−High ATF5−Low
Group
TTN 35%
PIK3CA 33%
KMT2C 22%
MUC16 20%
MUC4 19%
KMT2D 17%
DMD 15%
EP300* 15%
FLG 15%
SYNE1 15%
FBXW7 15%
LRP1B 13%
MUC17 13%
RYR2* 13%
USH2A 13%
ADGRV1 12%
CSMD1 12%
HUWE1 11%
PCLO* 11%
SYNE2 11%
NAV3 11%
DST 10%
MUC5B 10%
OBSCN 9%
AHNAK2* 9%
DNAH2 9%
EYS 9%
LRP2 9%
MDN1 9%
NEB 9%
Gene Type
Oncogene
TSG
Unknown
Group
ATF5−High
ATF5−Low
TCGA−CESC (Alterations)
Splice Site
Missense
Frameshift
Inframe ins/del
Nonsense
F
ATF4
G
NRF1
H
CLPP
I
HSPD1
J
HSPE1
K
GPX1
L
GPX4
M
SOD1
Expression: log2(FPKM+1)
N
Mutation of EP300
ATF5
Mitochondrial Stress Response Genes
Chemotherapeutic Resistance
Imatinib Sensitivity

◂ **Fig. 8** Identification of potent drugs based on *ATF5* expression levels. **A**–**D** Box plots exhibit drug IC50 values of cisplatin (**A**), paclitaxel (**B**), etoposide (**C**), and imatinib (**D**) in CESC group with high *ATF5* and low *ATF5*. **E** Mutational landscape of top 30 CESC driver genes of *ATF5*-High vs. *ATF*-Low. *$p < 0.05$ between two groups evaluated by Fisher's exact test. **F**–**M** Box plots comparing expression levels of *ATF4* (**F**), *NRF1* (**G**), *CLPP* (**H**), *HSPD1* (**I**), *HSPE1* (**J**), *GPX1* (**K**), *GPX4* (**L**), and *SOD1* (**M**) of *ATF5*-high vs. ATF-low patient groups. *$p < 0.05$, **$p < 0.01$, ***$p < 0.001$, ****$p < 0.0001$ between two groups evaluated by Wilcoxon test. **N** An integrated model illustrating the impact of ATF5 expression on drug sensitivity and its underlying molecular mechanisms

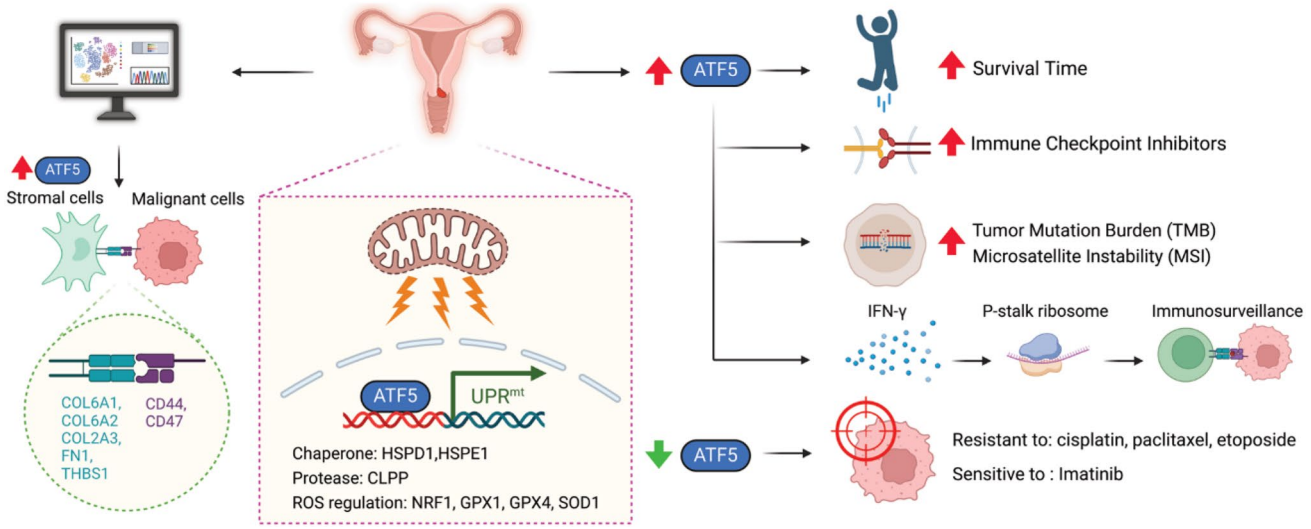

Fig. 9 A comprehensive schematic representation summarizing the novel role of *ATF5* in bridging the clinical significance of CESC with the basic biology of mito-nuclear communication. Central Panel: In the context of CESC progression, *ATF5* functions as a key transcription factor regulating the UPR^{mt} by orchestrating the transcription of specific genes involved in chaperone activity, protease function, and ROS regulation. Right Panel: Elevated *ATF5* levels correlate with longer survival times and are associated with increased expression of immune checkpoint inhibitors, tumor mutation burden (TMB), and microsatellite instability (MSI). Importantly, *ATF5* expression may influence the interferon-P-stalk ribosome-immunosurveillance axis. Furthermore, reduced *ATF5* levels confer resistance to the chemotherapeutics cisplatin, paclitaxel, and etoposide, while increasing sensitivity to imatinib. Left Panel: Single-cell RNA sequencing analysis reveals that stromal cells contribute to increased ATF5 expression levels and represent the major population interacting with malignant cells via COL6A1–CD44, COL6A2–CD44, COL6A3–CD44, FN1–CD44 and THBS1–CD47

studies, and functional assays in cellular models, will be essential to elucidate the precise molecular mechanisms underlying these associations and validate their biological significance in cervical cancer progression.

In conclusion, our findings reveal that high *ATF5* expression is associated with an immunologically active tumor microenvironment, characterized by increased immune cell infiltration and elevated immune checkpoint expression. This suggests that targeting *ATF5* may enhance the efficacy of immune checkpoint inhibitors by further amplifying anti-tumor immune responses. Moreover, *ATF5* expression appears to modulate tumor sensitivity to chemotherapy, with high *ATF5* levels correlating with improved responsiveness to agents like cisplatin, paclitaxel, and etoposide. These dual roles of *ATF5*—enhancing immune activity and sensitizing tumors to chemotherapy—underscore its potential as a key player in combination treatment strategies. By combining *ATF5*-targeted therapies with immune checkpoint inhibitors or standard chemotherapeutics, it may be possible to achieve synergistic effects, improving outcomes for patients with CESC.

Author contributions Conceptualization: H.-Y.L. and Y.-H.C.; methodology: H.-Y.L. and Y.-H.C.; software: H.-Y.L.; validation: K.-S.L.; formal analysis: H.-Y.L., Y.-H.C. and K.-S.L.; investigation: H.-Y.L. and Y.-H.C.; resources: K.-S.L. and Y.-H.C.; data curation: H.-Y.L. and Y.-H.C.; visualization: H.-Y.L. and H.-J.W.; writing—original draft preparation and H.-J.W.: H.-Y.L.; writing—review and editing: K.-S.L. and H.-J.W.; supervision: K.-S.L.; project administration: H.-Y.L. All authors have read and agreed to the published version of the manuscript.

Funding This study was supported by grants NSTC 112-2314-B-442-003- (recipient H.-Y.L.) and NSTC 113-2314-B-442-002- (recipient: H.-Y.L.) from the National Science and Technology Council, Taiwan, as well as by Show Chwan Memorial Hospital, Taiwan (SRD-112029, recipient: K.-S.L.). It is important to note that the funding organizations had no involvement in the study design, data collection, analysis, interpretation, manuscript writing, or the decision to submit this paper for publication.

Data availability The datasets supporting the conclusions of this article are included within the article.

Declarations

Consent for publication All the authors consent to publish this work.

Use of artificial intelligence tools During the preparation of this manuscript, we utilized artificial intelligence (AI) tools to enhance the quality and readability of the text. Specifically, GPT-4o was employed for sentence refinement, grammatical correction, and proofreading. This tool facilitated clarity, consistency, and overall linguistic precision. After applying these AI-assisted processes, the authors thoroughly reviewed and edited the content as required to align with the scientific rigor and purpose of the study, taking full responsibility for the integrity and accuracy of the final text. No AI-generated text or content was used without detailed verification and necessary modifications by the authors.

Competing interests The authors declare no competing interests.

Open Access This article is licensed under a Creative Commons Attribution-NonCommercial-NoDerivatives 4.0 International License, which permits any non-commercial use, sharing, distribution and reproduction in any medium or format, as long as you give appropriate credit to the original author(s) and the source, provide a link to the Creative Commons licence, and indicate if you modified the licensed material. You do not have permission under this licence to share adapted material derived from this article or parts of it. The images or other third party material in this article are included in the article's Creative Commons licence, unless indicated otherwise in a credit line to the material. If material is not included in the article's Creative Commons licence and your intended use is not permitted by statutory regulation or exceeds the permitted use, you will need to obtain permission directly from the copyright holder. To view a copy of this licence, visit http://creativecommons.org/licenses/by-nc-nd/4.0/.

References

1. Sung H, Ferlay J, Siegel RL, Laversanne M, Soerjomataram I, Jemal A, et al. Global cancer statistics 2020: GLOBOCAN estimates of incidence and mortality worldwide for 36 cancers in 185 countries. CA Cancer J Clin. 2021;71(3):209–49.
2. Zhang X, Fan Y, Tan K. A bird's eye view of mitochondrial unfolded protein response in cancer: mechanisms, progression and further applications. Cell Death Dis. 2024;15(9):667.
3. Wang G, Fan Y, Cao P, Tan K. Insight into the mitochondrial unfolded protein response and cancer: opportunities and challenges. Cell Biosci. 2022;12(1):18.
4. Inigo JR, Kumar R, Chandra D. Targeting the mitochondrial unfolded protein response in cancer: opportunities and challenges. Trends Cancer. 2021;7(12):1050–3.
5. Sears TK, Angelastro JM. The transcription factor ATF5: role in cellular differentiation, stress responses, and cancer. Oncotarget. 2017;8(48):84595–609.
6. Gho JW, Ip WK, Chan KY, Law PT, Lai PB, Wong N. Re-expression of transcription factor ATF5 in hepatocellular carcinoma induces G2-M arrest. Cancer Res. 2008;68(16):6743–51.
7. Wu Y, Wu B, Chen R, Zheng Y, Huang Z. High ATF5 expression is a favorable prognostic indicator in patients with hepatocellular carcinoma after hepatectomy. Med Oncol. 2014;31(11):269.
8. Uhlen M, Zhang C, Lee S, Sjostedt E, Fagerberg L, Bidkhori G, et al. A pathology atlas of the human cancer transcriptome. Science. 2017;357(6352):eaan2507.
9. Uhlen M, Fagerberg L, Hallstrom BM, Lindskog C, Oksvold P, Mardinoglu A, et al. Proteomics. Tissue-based map of the human proteome. Science. 2015;347(6220):1260419.
10. Liu CJ, Hu FF, Xie GY, Miao YR, Li XW, Zeng Y, et al. GSCA: an integrated platform for gene set cancer analysis at genomic, pharmacogenomic and immunogenomic levels. Brief Bioinform. 2023;24(1):bbac558.
11. Liao C, Wang X. TCGAplot: an R package for integrative pan-cancer analysis and visualization of TCGA multi-omics data. BMC Bioinform. 2023;24(1):483.
12. Lin A, Qi C, Wei T, Li M, Cheng Q, Liu Z, et al. CAMOIP: a web server for comprehensive analysis on multi-omics of immunotherapy in pan-cancer. Brief Bioinform. 2022;23(3):bbac129.
13. Han Y, Wang Y, Dong X, Sun D, Liu Z, Yue J, et al. TISCH2: expanded datasets and new tools for single-cell transcriptome analyses of the tumor microenvironment. Nucleic Acids Res. 2023;51(D1):D1425–31.
14. Li C, Guo L, Li S, Hua K. Single-cell transcriptomics reveals the landscape of intra-tumoral heterogeneity and transcriptional activities of ECs in CC. Mol Ther Nucleic Acids. 2021;24:682–94.
15. Hayashi A, Ruppo S, Heilbrun EE, Mazzoni C, Adar S, Yassour M, et al. GENI: A web server to identify gene set enrichments in tumor samples. Comput Struct Biotechnol J. 2023;21:5531–7.
16. Li K, Yang H, Lin A, Xie J, Wang H, Zhou J, et al. CPADS: a web tool for comprehensive pancancer analysis of drug sensitivity. Brief Bioinform. 2024;25(3):bbae237.
17. Dopler A, Alkan F, Malka Y, van der Kammen R, Hoefakker K, Taranto D, et al. P-stalk ribosomes act as master regulators of cytokine-mediated processes. Cell. 2024;187(24):6981-93 e23.
18. Li S, Shi J, Wang L, Zhang D, Zhang H. EP300 promotes lung cancer cell proliferation by regulating the oncogenic transcription of Hippo-YAP signaling pathway. Biochem Biophys Res Commun. 2024;692: 149330.

19. Vitiello GA, Medina BD, Zeng S, Bowler TG, Zhang JQ, Loo JK, et al. Mitochondrial inhibition augments the efficacy of imatinib by resetting the metabolic phenotype of gastrointestinal stromal tumor. Clin Cancer Res. 2018;24(4):972–84.
20. Zhou J, Tian H, Zhi X, Xiao Z, Chen T, Yuan H, et al. Activating transcription factor 5 (ATF5) promotes tumorigenic capability and activates the Wnt/b-catenin pathway in bladder cancer. Cancer Cell Int. 2021;21(1):660.
21. Luo Y, Lv B, He S, Zou K, Hu K. Identification of gene as predictive biomarkers for the occurrence and recurrence of osteosarcoma. Int J Gen Med. 2021;14:1773–83.
22. Hu M, Li H, Xie H, Fan M, Wang J, Zhang N, et al. ELF1 transcription factor enhances the progression of glioma via ATF5 promoter. ACS Chem Neurosci. 2021;12(7):1252–61.
23. Pang X, Li F, Lu M, Zhu L. Coordination of single-cell and bulk RNA sequencing to construct a cuproptosis-related gene prognostic index for endometrial cancer prognosis, immune microenvironment infiltration, and immunotherapy treatment options. J Cancer. 2023;14(16):3078–98.
24. Valenzuela Alvarez MJP, Gutierrez LM, Bayo JM, Cantero MJ, Garcia MG, Bolontrade MF. Osteosarcoma cells exhibit functional interactions with stromal cells, fostering a lung microenvironment conducive to the establishment of metastatic tumor cells. Mol Biol Rep. 2024;51(1):467.
25. Hartmann KP, van Gogh M, Freitag PC, Kast F, Nagy-Davidescu G, Borsig L, et al. FAP-retargeted Ad5 enables in vivo gene delivery to stromal cells in the tumor microenvironment. Mol Ther. 2023;31(10):2914–28.
26. Gabai Y, Assouline B, Ben-Porath I. Senescent stromal cells: roles in the tumor microenvironment. Trends Cancer. 2023;9(1):28–41.
27. Huo J, Guan J, Li Y. Metabolism reprogramming signature associated with stromal cells abundance in tumor microenvironment improve prognostic risk classification for gastric cancer. BMC Gastroenterol. 2022;22(1):364.
28. Gronkowska K, Robaszkiewicz A. Genetic dysregulation of EP300 in cancers in light of cancer epigenome control - targeting of p300-proficient and -deficient cancers. Mol Ther Oncol. 2024;32(4): 200871.

Publisher's Note Springer Nature remains neutral with regard to jurisdictional claims in published maps and institutional affiliations.